Molecular Dynamics Simulations of a Conformationally Mobile Peptide-Based Catalyst for Atroposelective Bromination

Xin Cindy Yan, **Anthony J. Metrano**, **Michael J. Robertson**, **Nadia C. Abascal**, **Julian Tirado–Rives**, **Scott J. Miller**[*], and **William L. Jorgensen**[*]

Department of Chemistry, Yale University, New Haven, Connecticut 06520-8107, USA

Abstract

It is widely accepted that structural rigidity is required to achieve high levels of asymmetric induction in catalytic, enantioselective reactions. This fundamental design principle often does not apply to highly selective catalytic peptides that often exhibit conformational heterogeneity. As a result, these complex systems are particularly challenging to study both experimentally and computationally. Herein, we utilize molecular dynamics simulations to investigate the role of conformational mobility on the reactivity and selectivity exhibited by a catalytic, β-turn-biased peptide in an atroposelective bromination reaction. By means of cluster analysis, multiple distinct conformers of the peptide and a catalyst-substrate complex were identified in the simulations, all of which were corroborated by experimental NMR measurements. The simulations also revealed that a shift in the conformational equilibrium of the peptidic catalyst occurs upon addition of substrate, and the degree of change varies among different substrates. On the basis of these data, we propose a correlation between the composition of the peptide conformational ensemble and its catalytic properties. Moreover, these findings highlight the importance of conformational dynamics in catalytic, asymmetric reactions mediated by oligopeptides, unveiled through high-level, state-of-the-art computational modeling.

Graphical Abstract

INTRODUCTION

Nature has evolved a diverse assortment of enzymes that catalyze biochemical reactions with superb efficiency and selectivity. The well-defined, folded structures of enzymes often contribute to their efficacy as catalysts by enabling their substrates to bind with high affinities and in precise orientations that ultimately give rise to highly stabilized transition states.[1] The design of small-molecule peptides that preserve key features of enzymatic active sites within a considerably simplified chiral environment has emerged as an effective strategy in the field of asymmetric catalysis.[2] Such oligopeptides present a variety of opportunities for catalyst development. The wide array of readily available amino acid residues makes peptidic catalysts quite modular and tunable. In addition, the high density of stereogenic centers and the myriad functional groups inherent to peptide sequences provide possibilities for multidentate interactions with the substrate, often through noncovalent interactions,[3] leading to significant stereo-, regio- and site-selectivity in catalytic reactions. [2,4] Over the years, peptide-based catalysts have been developed for a variety of mechanistically distinct, asymmetric reactions, including oxidations,[5] reductions,[6] group transfers,[7] and C–C bond forming reactions,[8] among others. Inspired initially by their ubiquity in biological systems and by their often predictable and well-characterized conformations,[9] β-turn motifs have emerged as promising scaffolds within catalytic peptides. The well-defined geometry of the β-turn, as well as the related β-hairpin,[10] has been found to be responsible for the efficient relay of stereochemical information during catalysis.[7,11]

Due to the close relationship between structure and activity of catalysts in asymmetric reactions, it has often been observed that highly selective catalysts are structurally quite rigid, as is the case with many chiral transition metal complexes, including the archetypical catalysts based on BINAP-type ligands among many others.[12,13] However, a number of recent studies show that very high levels of enantioselectivity can be achieved with organocatalysts that are themselves flexible.[14] These studies reveal that a variety of conformational states can coexist in solution and that the presence of a substrate can trigger

a shift in the conformational equilibrium toward a geometry that stabilizes catalyst-substrate interactions in a manner analogous to allosteric enzymes. Recent findings by Jacobsen and co-workers also underscore that a small-molecule catalyst may interact with multiple states along a complex reaction coordinate.[15,16]

Structural studies of designed tetrapeptides that exhibit β-turn secondary structures have shed new light on the importance of catalyst dynamics. These tetrapeptides often share an internal Pro–Xaa sequence, where Pro is D- or L-proline, and Xaa is a locally achiral, α,α-disubstituted amino acid. We recently expanded the purview of Pro–Xaa peptide-based catalysts to include the atroposelective bromination of 3-arylquinazolin-4(3H)-ones (e.g., **1**) to the corresponding tribromides (e.g., **2**) with high levels of enantioselectivity (Scheme 1).[17] Using a combination of X-ray crystallography, NMR spectroscopy, and DFT computational techniques, the study revealed 53 discrete peptide conformational states for 35 unique sequences that span a diverse range of ground state structures beyond what might have been originally expected from the design principles.[18] Moreover, conformational changes induced by substrate association were also observed through NMR titration experiments. Nevertheless, these experimental techniques could only offer limited information on stationary conformations or averaged structural signals, while a more detailed assessment of conformational mobility, transition dynamics, and substrate binding remained elusive.

Among catalytic peptides examined, peptide **3** stands out as a particularly interesting system owing to its ability to provide high levels of enantioselectivity despite its demonstrated structural flexibility.[17,18] The primary sequence of the peptide contains a catalytically active, tertiary amine-containing L-β-dimethylaminoalanine (Dmaa) residue at the N-terminal position and a β-turn-biasing D-Pro-Acpc (Acpc = 1-aminocyclopropyl-1-carboxamide) sequence in the loop region. Three distinct conformers of **3** were observed crystallographically (Figure 1). Conformers **3a** and **3b**, which are both characterized as type II′ β-hairpins, differ primarily in their degree of backbone bending, while conformer **3c** displays a pre-helical type I′ β-turn geometry. NMR analyses suggest that multiple conformations of the peptide may be populated simultaneously in solution under catalytically relevant conditions.

Different substrates are processed by catalyst **3** with varying levels of enantioselectivity.[17] The substituent at the 2-position of the quinazolinones scaffold, in particular, is shown to have a significant effect on the atroposelective bromination reaction. As shown in Scheme 1, while peptide **3** is able to process quinazolinone **1a** (R = Me) with high levels of enantioinduction, the substrate **1b** (R = CF$_3$) is significantly less selective under these conditions. Thus, it seems that the electrostatic perturbation in the substrate is responsible for the poorer selectivity observed with **1b**. Additionally, the appearance of intermolecular nOes and changes in the intramolecular signals were observed when different substrates were added to a solution of peptide **3**. Specifically, when associated with **1a**, the conformational profile of **3** becomes more homogeneous compared to the peptide alone; however, the opposite trend is observed in the presence of **1b**.[18]

Though such dynamic aspects of peptide-based catalysts have been proposed to be important to the mode of binding and activation, experimental study of these subtle mechanistic details remain elusive. Computational modeling can provide atomic-level descriptions for catalyst design and structure-function relationships.[19] Of course, many challenges currently exist, including the particular difficulty associated with modeling dynamic systems that populate multiple conformations in the ground state, as well as in reaction transition states.[20,21] Nonetheless, significant insight can be derived from multiparameter analysis of features associated with the substrates and catalysts.[22] In fact, it is even possible to correlate selectivity outcomes with different conformations of the same catalyst, suggesting that different transition state ensembles can contribute to the overall selectivity.[23] Yet, the explicit treatment of the conformational dynamics in such flexible catalysts remains a tremendous challenge and currently represents a gap in the field.

Herein, we utilize molecular dynamics simulations to investigate the conformational dynamics and substrate binding of peptide **3** with an emphasis on understanding their roles in asymmetric catalysis. The effects of substrate association and detailed binding mechanisms were explored through the comparative study of substrates **1a** and **1b** as they each dock with **3**. The present study makes extensive use of multidimensional clustering techniques to analyze the conformational states and catalyst-substrate complexes from simulation trajectories. Various through-space interaction distances were compared to the solution phase NMR measurements to validate the computational predictions and unravel the complexity inherent to the experimental observations. These results provide opportunities to expand understanding of the role of dynamics in peptide-based catalysts and showcase the potential application of state-of-the-art computation in catalyst design, optimization, and study.

METHODS

Molecular dynamics (MD) simulations were carried out using the NAMD software package version 2.10 with CUDA GPU acceleration.[24, 25] OPLS-AA/M force field parameters were used to describe the peptide;[26] the OPLS-AA force field[27] together with the 1.14*CM1A-LBCC charge models[28, 29] were used for solvent and substrate molecules. The development of OPLS-AA/M force field parameters for the Dmaa χ_1 dihedral and the Acpc backbone dihedrals based on QM calculations is described in the Supporting Information. In each simulation, the solute was solvated in a large cubic cell of organic solvent with length of box edges ranging from 32 to 35 Å, and subject to periodic boundary conditions. For all simulations, a temperature of 300 K and pressure of 1 atm were maintained using the Langevin thermostat with a damping coefficient of 1 ps^{-1} and Nose–Hoover Langevin piston barostat[30] with a piston period of 100 fs and a damping time scale of 50 fs. The Lennard–Jones (LJ) interactions were truncated at 12 Å with a smoothing function beginning at 10 Å. The particle-mesh Ewald (PME) method was used to treat long-range electrostatic interactions.[31] During the simulation, a 2 fs integration step was employed in conjunction with the SHAKE algorithm to constrain all covalent bonds containing hydrogen atoms.[32]

Two organic solvents, benzene and chloroform, were used for the MD simulations of the peptide alone. In each solvent system, MD simulations were performed starting from the

crystal structures of conformers **3a**, **3b**, and **3c**. The systems were first energy minimized for 5000 steps, and then the solvent was equilibrated for 500 ps before a full equilibration of the entire system over 5 ns. Finally, three replicate 200 ns production runs with different initial velocity assignments were performed, adding up to an aggregated simulation trajectory of 600 ns per starting conformer and 1.8 μs per solvent.

Simulations of the peptide-substrate complexes (**3+1a** and **3+1b**) were carried out in benzene. Each atropisomeric form of the quinazolinone substrates (a*R*- or a*S*-configuration about the chiral anilide bond) was separately subjected to the MD simulations in order to explore possible origins of the observed enantioselectivity in the atroposelective bromination reaction.[17] The initial structures of the complexes were prepared by docking the substrate with each of the three crystallographic conformations of **3** using AutoDock Vina.[33] The nine highest-ranked catalyst-substrate complexes were post-ranked based on the computed binding energies from conjugate gradient optimization and molecular mechanics (MM) calculations, as well as the root mean square errors (RMSE) of intermolecular nOe distances relative to experimental data. The best binding pose overall was selected for MD simulations, during which the solvent was first equilibrated for 500 ps while the geometry of the complex was fixed. The entire system subsequently underwent two stages of 500 ps equilibration with 10 and 5 kcal/mol nOe harmonic restraints on key interaction pairs corresponding to through-space interactions. Lastly, the equilibration was extended by 5 ns before three replicas of 200 ns production were run.

Multidimensional cluster analyses were employed to identify unique conformational states of the peptide from MD simulation trajectories. The clustering was based on various structural descriptors, including the backbone dihedral angles ϕ and ψ of the loop region residues (D-Pro and Acpc), the root-mean-square deviation (RMSD) of the structure with respect to the crystallographic geometry of the three conformers, the donor-acceptor distances of H-bonding pairs, the virtual dihedral angle (ϖ) comprised by the α-carbon atoms of the four residues, and the degree of backbone bending at *N*- and *C*-termini (Figure S3). Each descriptor serves as one dimension in the vector space that characterizes the structure at a certain point in time, while a 200 ns simulation trajectory contains 100,000 such snapshots. The vectors were normalized by each dimension to ensure all descriptors weigh equally in Euclidean space. The clustering was performed using the k-means++[34] and BIRCH[35] algorithms implemented in the scikit-learn machine learning package.[36] The number of clusters and clustering parameters were chosen to ensure that the separation coefficient of the resulting clusters is less than 0.3.[37] If a cluster was not sufficiently homogenous, clustering was repeated using additional descriptors such as the RMSD of residues or a subset of descriptors to further divide the cluster into unique subclusters. The centroid of each cluster was computed as the average of all data points (snapshots) in the cluster. Subsequently, the clusters formed were matched to known conformers from crystallographic studies based on the centroid coordinates; otherwise, the cluster was identified as a new unique conformer. The cluster analysis and conformation identification were performed on a trajectory-by-trajectory basis, and the overall results were then combined for each system. Cluster techniques were also applied to categorize the binding poses of substrates, for which the RMSD of the substrate and the geometric centers of the

phenol and benzo moieties of **1** were chosen as the clustering criteria. A maximum separation coefficient of 0.4 was used for clustering due to larger variations in the binding geometries. Once the binding poses were categorized, the conditional probability for the occurrence of a peptide conformer given a specific binding pose as well as ensemble averaged through-space distances of atom pairs were computed according to methods specified in the Supporting Information.

RESULTS & DISCUSSION

Peptide Conformations in the Absence of Substrates.

Key structural features were analyzed based on 1.8 μs of aggregated MD simulation results for peptide **3** in benzene. Figure 2 shows the joint distributions of backbone dihedral angles ϕ and ψ in the loop region colored by density. Two regions of high probability are observed in the neighborhood of the crystal values in each ϕ,ψ plot. However, the distributions around the crystal values of conformers **3a** and **3b** appear to have merged into a single peak with a significantly lower intensity than the one near the crystallographic values of **3c**. The center of the distribution at large, positive ϕ values of the i+2 residue are in close agreement with the optimized geometry from MM calculations (Table S2), while deviating from the crystallographic value of **3c** by about 15°. It is noteworthy that the four major joint distributions span a region of 20–50° in each dimension, suggesting that there is still structural flexibility around the local minima despite the general tendency for the peptide to fold into stable secondary structures. The histograms in Figure S4 illustrate the intramolecular H-bonding distances between the donor-acceptor pairs. Although the majority of the H-bond length distributions are in the vicinity of the crystal values, additional peaks appear at longer distances of $N(i)\cdots O(i+3)$ and $N(i+3)\cdots O(i)$. Given that these H-bonding pairs are located within the terminal residues, it can be inferred that the distal regions of the peptide undergo larger structural movements in the simulations. Figure S5 shows a series of histograms of the virtual dihedral angle ϖ, which is comprised by the α-carbons of each of the four residues, and dihedral angles $\phi(i)$ and $\phi(i+3)$ that characterize the bending of terminal residues. Most of the torsional angle distributions from the simulations are in accord with the crystallographic observations. In the plots of ϖ and $\phi(i+3)$, one crystallographic measurement disappears in the simulations, while an additional peak arises, suggesting the occurrence of new conformers.

Cluster analysis was performed on the MD simulation trajectories, and the various clusters generated were either associated with known conformers or classified as new ones. Overall, four primary conformers were identified from the clustering. Among them, two of the conformers correspond to **3a/b** (Figure 3a) and **3c** (Figure 3b), respectively. There was no statistically significant structural distinction between conformers **3a** and **3b** in the cluster analysis. The mean and one standard deviation of the geometric descriptors for each conformer are reported in Tables S5 and S6, together with the crystallographic measurements. For conformer **3a/b**, the two H-bonds, $NH(i+3)\cdots O(i)$ and $NH(i)\cdots O(i+3)$, that stabilize the β-hairpin secondary structure, are maintained in the simulations. The cluster average of virtual dihedral ϖ exhibits better agreement with the conformer in the crystal structure of **3a** than the more twisted geometry observed in **3b**. For the cluster that

corresponds to conformer **3c**, all geometric properties compare well with the crystallographic data. In addition to the two stable H-bonds, NH(i+3)···O(i) and NH(i+2)···O(i−1), it is interesting to note that the close contact between N(i) and O(i+3) as observed in the DFT and MM optimizations (Table S3), turns out to be unstable in the simulations. This suggests that this H-bond might be enthalpically stable but entropically disfavored. Two additional conformers, **3d**, which resembles **3c**, and a new, unique conformation **3e**, are also found in simulations (Table S7, S8). As illustrated in Figure 3b, conformer **3d** differs from **3c** primarily by a 55° rotation about the backbone dihedral ψ(i+3). Due to this change, the distance between N(i) and O(i+3) increases by 3 Å with respect to conformer **3c**, and the virtual dihedral ϖ is ~20° more twisted. In comparison, the geometric distinction between **3e** (Figure 3c) and the other three conformers is more pronounced. As shown in Figure 4, the loop dihedrals ϕ,ψ(i+1) of **3e** are located in a similar region as those of **3c**, while ϕ,ψ(i+2) more closely resemble conformer **3a/b**. This unique preference of the dihedrals does not match any of the canonical β-turn potentials.[9] Short contacts between NH(i+2)···O(i−1) and NH(i+2)···O(i) are observed in **3e**, although the first pair complies better with the ideal directionality of H-bonding.[38] Conformer **3e** exhibits a positive and notably twisted virtual dihedral ϖ.

Figure 5a shows the conformational composition of peptide **3** from the clustering analysis of aggregated simulation trajectories, as well as from each starting geometry, **3a**, **3b**, or **3c**. The pie charts of the global average demonstrate that **3c** is the predominant conformation in simulations of the free peptide in benzene solution, accounting for about 75% of the overall population. The second largest cluster belongs to **3e** (19%), which is followed by a much smaller share (5%) of corresponding to conformer **3a/b**. The remaining ~1% of the population are divided between the **3d** conformer and others. Analyzing the population according to the starting conformation shows that the results are generally independent of the starting geometry. Consistent with the global average, conformer **3c** dominates each individual average, and the trajectories starting from conformers **3a** or **3b** do not seem to bias the population towards the initial geometry. Overall, the simulation results support the experimental observation of multiple conformational states in solution. The simulation results of peptide **3** alone in chloroform can be found in the Supporting Information.

Peptide Conformations in the Presence of Substrate 1a.

To study the effects of substrate binding on the dynamics of the catalytic peptide, MD simulations were carried out for 1:1 mixtures of **3** and quinazolinone **1a** in benzene. Although the rotational barrier about the chiral anilide axis of **1a** is expected to be quite low (~19 kcal/mol),[17] **1a** was predisposed in the (aS)-configuration for the simulations, in accordance with the observed absolute configuration of the product, **2a**. It is noteworthy that no enantiomerization from (aS) to (aR) was observed over the course of the simulations. The joint distributions of the loop region dihedral angles ϕ and ψ reveal a substantial population shift in simulations of the 1:1 mixture from those of the peptide alone (Figure 6). Specifically, the region that corresponds to the type II′ β-hairpin conformation (i.e., **3a/b**) becomes much more densely populated than the prehelical, type I′ β-turn conformation (i.e., **3c**) in the presence of (S)-**1a**. Nevertheless, the locations and variances of the distributions are quite similar in simulations with and without the substrate. Analogous

distributional changes are observed in the histograms of other characteristic dihedral angles (Figure S5). Again, the peaks occur in similar positions for simulations in the presence and absence of the substrate, but the intensities are rather different. In simulations of the 1:1 mixture, the distributions of H-bonding pairs also change in favor of a close contact between N–H(i)⋯O(i+3), while weakening the NH(i+2)⋯O(i–1) interaction that stabilizes the prehelical conformation (Figure S4).

The results of the cluster analyses are reported in Tables S5, S6, and S8. Three distinct clusters that correspond to conformers **3a/b**, **3c**, and **3e** are identified from the simulations. The geometric descriptors in each cluster take nearly identical mean values to those in the substrate-free simulations, while the standard deviations are found to be smaller. Notable changes are found in the composition of conformers upon the addition of the substrate. As shown in Figure 5b, conformer **3a/b** becomes significantly stabilized in the presence of (aS)-**1a**, comprising 75% of the entire population. In contrast, the formerly predominant conformer **3c** is reduced to 19%, while conformer **3e** takes 5% among the remains. Again, the cluster results computed for trajectories with different starting geometries reveal comparable compositions. It is important to note that there is still a 62% chance that the peptide will take the **3a/b** conformation, even when starting from **3c**. These results imply that the presence of substrate considerably alters the conformational landscape of the peptide, shifting the secondary structural equilibrium towards conformer **3a/b** and away from **3c**.

Substrate Binding Mechanism and Impact on Peptide Dynamics.

To investigate how substrate **1a** associates with peptide **3**, a multidimensional cluster analysis was performed to identify the major binding orientations. Visualization of the simulation trajectories shows that the movement of the substrate is much more pronounced than that of the peptide; **1a** is constantly associating with and dissociating from **3**. These dynamics are accompanied by changes in intermolecular interactions. Some key intermolecular distances in various binding poses of the **3+1a** complex are summarized in Table 1. Among all clusters, pose A demonstrates short intermolecular contacts and the smallest standard deviations, indicating tight binding. In other poses, the intermolecular contacts occur at much longer distances and have larger variation. Structural inspection confirms that the peptide–substrate association is looser, or more dissociative, in poses B–I and is more susceptible to thermal fluctuations. The heatmap of intermolecular contacts between substrate atoms and peptide residues (Figure S10) for each cluster reveals a diverse array of binding mechanisms. Population analysis shows that pose A occupies the largest percentage of 39% (Figure 7a), confirming that it is the most stable binding mode among all alternatives.

Figure 7c depicts a representative snapshot of the **3+1a** complex in pose A, in which the binding pattern of the complex is found to be very similar to the one proposed based on the experimental observations.[17] Specifically, the substrate interacts with the peptide in a multidentate mode, with H-bonds formed between the phenol of the substrate and the Brønsted basic tertiary amine moiety of peptide **3**, as well as between the carbonyl of the quinazolinone and the backbone amide N–H bond of the Acpc residue. These interactions

corroborate the downfield shifts of the N*H*(Acpc) and α-C*H*/β-C*H₂*(Dmaa) signals in NMR titration experiments.[17,18] The phenol ring of the substrate is disposed directly above α-H of the *i*+1 D-Pro residue, which corroborates the upfield shift of this NMR signal in the titration experiments, possibly due to anisotropic effects. Moreover, pose A shows that the *ortho*-C-atom of **1a** is oriented in close proximity to the peptide backbone, as evidenced by the close contacts between α(D-Pro) of **3** and H*ortho* of **1a**. As this position has been shown to be the site of stereodetermining bromination,[17] these data are possibly consistent with a mechanism of bromination wherein peptide **3** delivers bromenium ion to **1a**, possibly with the aid of the proximal Lewis basic carbonyls.[39] The benzo ring of the quinazolinone substrate is situated above the Leu residue, which might also explain the upfield shifts of multiple Leu signals caused by the arene ring current when the substrate is added to the solution.

Typically, the peptide is found to adopt a type II′ β-hairpin conformation when the substrate is in pose A. Quantitative analysis shows that the probability of the peptide being in conformation **3a/b** when pose A occurs is 98%, revealing a close correlation between the binding mechanism and peptide conformational dynamics. Visualization of the MD simulation trajectories suggests that the substrate associates with the peptide in a manner similar to an "induced fit" model.[1] The close contacts between the peptide and the substrate encourage $\phi(i+2)$ to adopt values consistent with the type II' β-turn conformation during the formation of the C=O(**1a**)···H–N(Acpc) H-bond. At the same time, the formation of the O–H(**1a**)··· NMe₂(Dmaa) and N–H(*i*)···O(*i*+3) H-bonds leads to a concerted rotation of the Dmaa side-chain. According to QM torsional scans of the peptide alone, the two-dimensional energy profile of $\phi,\psi(i+2)$ is generally symmetric between the canonical values of type I' and II' β-turn structures. The binding of the substrate breaks this symmetry and bias the peptide conformation in favor of type II' β-hairpin secondary structure (Figure S2).

Effects of Substrates on Peptide Dynamics and Catalytic Activity.

Previous experimental studies show that peptide **3** catalyzes the bromination of multiple substrates with varying levels of enantioselectivity. Of the 14 substrates examined initially, only quinazolinone **1b**, which possesses a trifluoromethyl group (CF₃) at the 2-position, was believed to give modest enantioselectivity (63:37 er) due to poor peptide–substrate association.[17] In the present study, simulations were carried out for the **3+1b** complex in benzene and compared with the results for **3+1a** to investigate the influence of substrates on peptide dynamics and catalytic activity. Again, **1b** was originally predisposed in the (a*S*)-configuration. The joint distributions of loop region dihedral angles ϕ and ψ of peptide **3** in the presence of (a*S*)-**1b** are plotted in Figure 8. The distributions populate similar regions as in the plots of the **3+1a** complex, although the density increases to some extent in the regions representing the prehelical, type I' β-turn geometry. Evidence that supports an increasing occurrence of conformer **3c** is also detected in histograms of N(*i*+2)···O(*i*−1) distances, virtual dihedral ϖ, and dihedral angle $\phi(i)$ (Figures S11 and S12). These observations are validated by the composition profile of conformers (Figure 5c), in which the percentage of conformer **3a/b** decreases from 75% in simulations of **3+1a** to 51% in the **3+1b** variant. Concurrently, the population of conformer **3c** and **3e** nearly doubled in the presence of substrate **1b**. Nevertheless, there is a high degree of similarity in structures of the same conformer among simulations with different substrates (Tables S5, S6, and S8).

The mechanism of association for the **3+1b** complex was studied *via* cluster analysis of the substrate and examining the binding pose in each cluster. Among the ten major clusters, pose A displays short contacts that are in line with catalyst–substrate titration studies.[18] Referring to the pie chart of the binding pose composition (Figure 7b), pose A accounts for 31% of the population, which is 8% lower than the proportion of the primary binding pose in the **3+1a** mixture. The composition analysis also reveals a higher occurrence of small clusters and the appearance of a larger, unclassified cluster. Structural overlay of the representative binding pose of **3+1a** and **3+1b** systems (Figure 7c) suggests that the binding sites, absolute stereochemical configuration of the substrate, and intermolecular interactions are highly conserved between the two poses. Specifically, the average intermolecular distances observed in pose A of the **3+1b** system (Table S9) compare well the corresponding values in the **3+1a** system, although the standard deviations are slightly higher. To summarize, the comparative study established that there is an increased structural diversity in the **3+1b** system, which is exhibited in both peptide conformational space and substrate association mechanisms. Based on the similarity in the bidentate binding pose of the complex in the two systems, we can hypothesize that the decrease in selectivity observed for substrate **1b** can be attributed mainly to the availability of multiple binding modes and weaker intermolecular association, which perhaps relate to the enhanced structural mobility of peptide **3** in the **3+1b** mixture. The poorer association may arise from either unfavorable electrostatic interactions between the CF_3 group of **1b** and the peptide backbone, poorer H-bonding between **3** and **1b** as a result of decreased Lewis basicity of the quinazolinone carbonyl, or a combination of the two.

Implications of Structural Dynamics on Enantioselectivity.

Based on DFT computed barriers to rotation about the chiral anilide axes of quinazolinones **1a** and **1b**,[17,40] substrate enantiomerization (i.e., atropisomerism) is expected to occur on the timescale of seconds (**1a**, $\Delta G^{\ddagger} = 18.8$ kcal/mol; **1b**, $\Delta G^{\ddagger} = 19.3$ kcal/mol), which is well beyond the length of the simulation. Thus, in order to investigate the mechanism of enantiodiscrimination, simulations of the (aS)- and (aR)-atropisomeric forms of substrates **1a** and **1b** were carried out separately. Figure S13 shows the joint distributions of loop region dihedral angles ϕ and ψ of peptide **3** in the presence of (aR)-**1a**. A major increase of population is observed in the vicinity of the prehelical, type I' β-turn secondary structure (e.g., **3c**), in comparison with the distribution of the (aS)-atropisomer (Figure 8). The population shift is also observed in the histograms of the N(i)···O(i+3) and O(i−1)···N(i+2) distances, twisting angle ϖ, and dihedral angle $\phi(i)$, suggesting that the individual atropisomers of **1a** induce very different distributions in the structural features of **3** (Figures S14 and S15). Evaluation of the conformer populations illustrates that there is a substantial enhancement in the structural diversity of the peptide in the **3**+(aR)-**1a** complex (Figure 5d). The population of conformer **3a/b** diminishes from 75% in the presence of (aS)-**1a** to 27% in the presence of the (aR)-atropisomer. In contrast, the percentage of conformer **3c** increases from 19% to 43%, making it the predominant conformer. Moreover, there is also a five-fold rise in the population of **3e** in the presence of (aR)-**1a** in comparison with its enantiomer.

As for the comparative study of **3**+(a*R*)-**1b** and **3**+(a*S*)-**1b** complexes, the differences in conformational ensembles are revealed to be much subtler. As shown in the joint distributions of loop dihedrals (Figure S16) and histograms of inter-residue distances and dihedrals (Figures S17, S18), both the locations and intensities of the distributions align very well between the two atropisomers of **1b**. These observations are further backed by the cluster results, which exhibit very similar conformational profiles; there is only a minor decrease in the population of conformer **3a/b** and an increase in unclassified conformations with (a*R*)-**1b** (Figure 5e). This lack of conformational differentiation between the atropisomers of **1b** may be a source of the poor selectivity observed in the **3**-catalyzed bromination of this substrate.

Important changes in the binding mechanism and strength of association were identified when the (a*R*)-atropisomers of **1a** or **1b** associate with the peptide. Cluster analysis of the binding poses shows that the (a*R*)-atropisomers tend to interact with peptide **3** with a higher level of heterogeneity than the (a*S*)-atropisomers. As shown in Figure S19, the percentage of unclassified binding poses increases from 15% and 25% in **3**+(a*S*)-**1a** and **3**+(a*S*)-**1b** systems, to 44% and 31%, respectively, in their (a*R*)-counterparts. Among all categorized binding poses with the (*R*)-atropisomers, pose A forms the most short, intermolecular contacts. However, both the averages and standard deviations of these intermolecular distances are 1–2 Å greater than in the corresponding pose with the (a*S*)-atropisomers (Tables S14 and S15). Visualization of the structures reveals that (a*R*)-**1a** and (a*R*)-**1b** associate with peptide **3** in very similar bidentate modes (Figure S19). In this binding pose, the peptide displays a β-hairpin secondary structure and the two intermolecular hydrogen bonds O–H(substrate)···NMe$_2$(Dmaa) and C=O(substrate)···NH(Acpc) are identical to those formed in the **3**+(a*S*)-**1a** and **3**+(a*S*)-**1b** complexes. However, the (a*R*)-atropisomers are unable to align the quinazolinone rings with the loop region residues, D-Pro and Acpc, to gain the additional hydrophobic stabilization observed in the (a*S*)-counterparts. Due to the different binding mode of the (a*R*)-**1a** and **1b**, pose A only accounts for 4% and 8% of the total population, respectively. The weaker peptide–substrate association in turn reduces the impact of substrate on peptide conformational landscape, giving rise to a higher degree of variability in the peptide geometry.

The results of computational modeling suggest that the enantioselectivity exhibited by catalytic peptide **3** is closely related to its structural dynamics, which in turn influences the precise mechanism of interaction with the substrate and the strength of that association. For a substrate to exhibit good levels of enantioselectivity in the atroposelective bromination reaction, a significant change in the conformational dynamics of peptide **3** is expected with respect to the discrete atropisomeric forms of the substrate.

Comparison with NMR Measurements.

The through-space distances of between pairs of protons were computed from MD simulations and compared to the corresponding solution phase nOe measurements.[18] The results for peptide **3** in benzene solution are reported in Figure 9a. A majority of the computed intramolecular distances agree well with those derived from NOESY experiments, which confirms that computer simulations describe a similar conformational ensemble as in

the NMR experiments. It is also noteworthy that the correlation is better for shorter-distance interactions. At larger distances, most of the through-space interactions involve multiple chemically-equivalent hydrogen atoms on the side-chains of the Dmaa or Leu residues, whose pairwise distances may vary widely depending on the precise orientation of the side-chain. Past research has shown that, in those scenarios, the effects from internal motion of the peptide will have a substantial impact on nOe measurements, thus making the r^{-6} averaging scheme in the current computation less accurate.[41, 42, 43] A detailed comparison of the through-space distances in each cluster is shown in Table S16. A closer examination of the table shows that a majority of the experimental observations decently corroborate the computed values from some individual clusters, and the alignment varies from case to case. For example, conformer **3a/b** satisfies the nOe measurements for NH(Dmaa)↔NH(Leu) and NH(Acpc)↔α(D-Pro) much better than others, while conformer **3c** fits the nOe signals of NH(Acpc)↔δ(D-Pro), Boc(Dmaa)↔β(Acpc). Other pairs, such as NH(Acpc)↔NH(Leu) and NH(Leu)↔α(D-Pro), are found to be consistent with all clusters. In general, all major conformers partially comply with the experimental nOe measurements, and no clear conclusions can be drawn about which one dominates the solution population. This comparison reinforces the claim that multiple conformers coexist in solution.[18]

Upon the addition of substrate (a*S*)-**1a**, reasonable correlations between the computed and experimental data have been identified (Figure 9a, Table S17). Notably, the significantly better alignments between conformer **3a/b** and nOe values for NH(Leu)↔NH(Dmaa), NH(Acpc)↔α(D-Pro), NH(Dmaa)↔Me$_2$N$_{cis}$(Leu), α(D-Pro)↔β(Acpc), and β(Dmaa) ↔α(Leu) supports the experimental statement that the peptide adopts a more organized, homogeneous conformation akin to type II′ β-hairpin. Meanwhile, there is still evidence for the presence of conformer **3c** due to agreements in through-space interactions, the computed values determined for most of the binding poses are much larger than the experimental estimates. The only exception is pose A, for which two-thirds of through-space interactions agree to the nOe values within 1 Å (Figure 9b). Particularly, close contacts between α(D-Pro)↔*ortho*-H(**1a**), β(Acpc)↔5-H(**1a**), and δ(Leu)↔6-H(**1a**) lend credence to the proposed association mechanism and distinguish pose A as the primary binding mode. The computed intramolecular through-space interactions for the **3**+(a*S*)-**1b** complex are compared to the NOE measurements (Figure 9a and Table S18). Excellent correlations with experimental values are observed for both the global averages and averages within each individual cluster, validating the hypothesis that the conformational profile of peptide **3** in the presence of **1b** is highly diverse. The predicted binding pose A is again validated by the NOESY distance comparison shown in Figure 9b, as the differences in most of the intermolecular distances are less than 0.5 Å. For complexes **3**+(a*R*)-**1a** and **3**+(a*R*)-**1b**, the computed intramolecular distances of the peptide compare reasonably with experimental values (Figure S20a, Tables S19, S20). However, large deviation from nOe measurement is found for intermolecular distances of peptide and the (a*R*)-quinazolinones in pose A (Figure S20b). These data confirm that the (a*R*)-atropisomer is the less favored substrate for binding and interaction with peptide **3**.

CONCLUSION

This study comprehensively and systematically examined the conformational dynamics of a β-turn-biased catalytic peptide (**3**) and its role in substrate binding and enantioinduction using computational modeling. By means of cluster analysis, multiple stable conformers have been identified from the MD simulations, including ones that were previously observed crystallographically and two that were heretofore unidentified. Despite the fact that simulations of the peptide alone and various peptide–substrate complexes share similar and well-defined conformers, the relative populations of conformers vary drastically across the different systems. For peptide **3**–substrate **1a** mixture, the conformational dynamics of the peptide are proposed to be quite important for catalytic activity and enantioselectivity in the atroposelective quinazolinones bromination reaction. Computational modeling also confirms the proposed association mechanism, in which the (a*S*)-enantiomer of the quinazolinones substrate binds favorably to the type II' β-hairpin conformer of the peptide **3** with bidentate H-bonding interactions. In the presence of **1b**, a poorly performing substrate, the enhanced structural mobility of the peptide and the smaller changes in conformational distribution from upon complexation with the (a*S*)- and (a*R*)-atropisomeric forms of the substrate are in line with the reduced yield and enantioselectivity observed in the catalytic reaction. Despite having a similar binding pose, the considerable differences in conformational dynamics between complexes **3+1a** and **3+1b** demonstrate that catalyst dynamics are important to enantioselectivity. Furthermore, the simultaneous existence of multiple conformers of peptide **3** and the optimal mode of substrate binding and activation are validated by the good correlation between the computed through-space interactions and NMR experimental values. Overall, the study highlights the fluxional nature of peptide-based catalysts and the crucial role of conformational dynamics in catalytic activity and enantioselectivity for this reaction. These results provide a detailed view of the advantages of flexible catalysts for asymmetric reactions. Notably, well-defined, rigid structures appear to play a role at various points in the reaction coordinate. Yet, MD simulations reveal that these structures may indeed differ substantially from those in a diverse conformational ensemble for the catalyst ground state. Overall, this study may provide a roadmap for the implementation of rigorous computational modeling of catalyst dynamics and may also enable more precise designs based on expanded understanding of the structure-function continuum.

Supplementary Material

Refer to Web version on PubMed Central for supplementary material.

Acknowledgements

REFERENCES

1. (a) Knowles JR Enzyme Catalysis: Not Different, Just Better. Nature 1991, 350, 121–124. [PubMed: 2005961] (b)Kirby AJ Enzyme Mechanisms, Models, and Mimics. Angew. Chem. Int. Ed 1996, 35, 706–724.(c)Zhang X; Houk KN Why Enzymes are Proficient Catalysts: Beyond the Pauling Paradigm. Acc. Chem. Res 2005, 38, 379–385. [PubMed: 15895975] (d)Smith AJT; Müller R; Toscano MD; Kast P; Hellinga HW; Hilvert D; Houk KN Structural Reorganization and Preorganization in Enzyme Active Sites: Comparisons of Experimental and Theoretically Ideal Active Site Geometries in the Multistep Serine Esterase Reaction Cycle. J. Am. Chem. Soc 2008, 130, 15361–15373. [PubMed: 18939839]

2. (a)For reviews, see: Miller SJ In Search of Peptide-Based Catalysts for Asymmetric Organic Synthesis. Acc. Chem. Res 2004, 37, 601–610. [PubMed: 15311959] (b)Colby Davie EA; Mennen SM; Xu Y; Miller SJ Asymmetric Catalysis Mediated by Synthetic Peptides. Chem. Rev 2007, 107, 5759–5812. [PubMed: 18072809] (c)Wennemers H Asymmetric Catalysis with Peptides. Chem. Commun 2011, 47, 12036–12041.(d)Lewandowski B Wennemers, H. Asymmetric Catalysis with Short-Chain Peptides. Curr. Opin. Chem. Biol 2014, 22, 40–46. [PubMed: 25277500]

3. (a)Doyle AG; Jacobsen EN Small-Molecule H-Bond Donors in Asymmetric Catalysis. Chem. Rev 2007, 107, 5713–5743. [PubMed: 18072808] (b)Knowles RR; Jacobsen EN Attractive Noncovalent Interactions in Asymmetric Catalysis: Links Between Enzymes and Small Molecule Catalysts. Proc. Natl. Acad. Sci. U.S.A 2010, 107, 20678–20685. [PubMed: 20956302] (c)Toste FD; Sigman MS; Miller SJ Pursuit of Noncovalent Interactions for Strategic Site-Selective Catalysis. Acc. Chem. Res 2017, 50, 609–615. [PubMed: 28945415] (d)Davis HJ; Phipps RJ Harnessing Non-Covalent Interactions to Exert Control Over Regioselectivity and Site-Selectivity in Catalytic Reactions. Chem. Sci 2017, 8, 864–877. [PubMed: 28572898]

4. (a)For reviews on site-selective catalysis, see: Giuliano MW; Miller SJ Site-Selective Reactions with Peptide-Based Catalysts. Top. Curr. Chem 2016, 372, 157–201. [PubMed: 26307403] (b)Shugrue CR; Miller SJ Applications of Non-Enzymatic Catalysts to the Alteration of Natural Products. Chem. Rev 2017, 117, 11894–11951. [PubMed: 28580785] (c)Hartwig JF Catalyst-Controlled Site-Selective Bond Activation. Acc. Chem. Res 2017, 50, 549–555. [PubMed: 28945414] (d)Huang Z; Dong G Site-Selectivity Control in Organic Reactions: A Quest to Differentiate Reactivity Among the Same Kind of Functional Group. Acc. Chem. Res 2017, 50, 465–471. [PubMed: 28945402]

5. (a)For select examples, see: Romney DK; Colvin SM; Miller SJ Catalyst Control over Regio- and Enantioselectivity in Baeyer-Villiger Oxidations of Functionalized Ketones. J. Am. Chem. Soc 2014, 136, 14019–14022. [PubMed: 25250713] (b)Alford JS; Abascal NC; Shugrue CR; Colvin SM; Romney DK; Miller SJ Aspartyl Oxidation Catalysts that Dial in Functional Group Selectivity, along with Regio- and Stereoselectivity. ACS Cent. Sci 2016, 2, 733–739. [PubMed: 27800556]

6. (a)Shugrue CR; Miller SJ Phosphothreonine as a Catalytic Residue in Peptide-Mediated Asymmetric Transfer Hydrogenations of 8-Aminoquinolines. Angew. Chem. Int. Ed 2015, 54, 11173–11176.(b)Shugrue CR; Featherston AL; Lackner RM; Lin A; Miller SJ Divergent Stereoselectivity in Phosphothreonine (pThr)-Catalyzed Reductive Aminations of 3-Amidocyclohexanones. J. Org. Chem 2018, 83, 4491–4504. [PubMed: 29547285]

7. (a)For select examples, see: Miller SJ; Copeland GT; Papaioannou N; Horstmann TE; Ruel EM Kinetic Resolution of Alcohols Catalyzed by Tripeptides Containing the *N*-Alkylimidazole Substructure. J. Am. Chem. Soc 1998, 120, 1629–1630.(b)Sculimbrene BR; Morgan AJ; Miller SJ Nonenzymatic Peptide-Based Catalytic Asymmetric Phosphorylation of Inositol Derivatives. J. Am. Chem. Soc 2002, 124, 11653–11656. [PubMed: 12296730] (c)Jordan PA; Miller SJ An Approach to the Site-Selective Deoxygenation of Hydroxyl Groups Based on Catalytic Phosphoramidite Transfer. Angew. Chem. Int. Ed 2012, 51, 2907–2911.

8. (a)For select examples, see: Mbofana CT; Miller SJ Diastereo- and Enantioselective Addition of Anilide-Functionalized Allenoates to N-Acyl Imines Catalyzed by a Pyridylalanine-Based Peptide. J. Am. Chem. Soc 2014, 136, 3285–3292. [PubMed: 24527787] (b)Kim B; Chinn AJ; Fandrick DR; Senanayake CH; Singer RA; Miller SJ Stereodynamic Quinone-Hydroquinone Molecules that Enantiomerize at sp^3-Carbon via Redox-Interconversion. J. Am. Chem. Soc 2016, 138, 7939–7945. [PubMed: 27254785] (c)Ryss JM; Turek AK; Miller SJ Disulfide-Bridged Peptides that Mediate Enantioselective Cycloadditions through Thiyl Radical Catalysis. Org. Lett 2018, 20, 1621–1625. [PubMed: 29504763]

9. (a)Sibanda BL; Thornton JM Nature 1985, 316, 170–174. β-Hairpin Families in Globular Proteins. [PubMed: 4010788] (b)Wilmot CM; Thornton JM Analysis and Prediction of the Different Types of β-Turn in Proteins. J. Mol. Biol 1988, 203, 221–232. [PubMed: 3184187] (c)Haque TS; Little JC; Gellman SH Stereochemical Requirements for β-Hairpin Formation: Model Studies with Four-Residue Peptides and Depsipeptides. J. Am. Chem. Soc 1996, 118, 6975–6985.

10. (a)Karle IL; Awasthi SK; Balaram PA Designed β-Hairpin Peptide in Crystals. Proc. Natl. Acad. Sci. U. S. A 1996, 93, 8189–8193. [PubMed: 8710845] (b)Aravinda S; Raghavender US; Rai R; Harini VV; Shamala N; Balaram P Analysis of Designed β-Hairpin Peptides: Molecular Conformation and Packing in Crystals. Org. Biomol. Chem 2013, 11, 4220–4231. [PubMed: 23680821]

11. (a)For select transformations employing β-turn-containing peptides as catalysts, see: Jarvo ER; Copeland GT; Papaioannou N; Bonitatebus PJ; Miller SJ A Biomimetic Approach to Asymmetric Acyl Transfer Catalysis. J. Am. Chem. Soc 1999, 121, 11638–11643.(b)Gilbertson SR; Collibee SE; Agarkov A Asymmetric Catalysis with Libraries of Palladium β-Turn Phosphine Complexes. J. Am. Chem. Soc 2000, 122, 6522–6523.(c)Krattiger P; Kovàsy R; Revell JD; Ivan S; Wennemers H Increased Structural Complexity Leads to Higher Activity: Peptides as Efficient and Versatile Catalysts for Asymmetric Aldol Reactions. Org. Lett 2005, 7, 1101–1103. [PubMed: 15760149] (d)Wiesner M; Revell JD; Tonazzi S; Wennemers H Peptide Catalyzed Asymmetric Conjugate Addition Reactions of Aldehydes to Nitroethylene—A Convienient Entry into γ^2-Amino Acids. J. Am. Chem. Soc 2008, 130, 5610–5611. [PubMed: 18386927] (e)Akagawa K; Akabane H; Sakamoto S; Kudo K Organocatalytic Asymmetric Transfer Hydrogenation in Aqueous Media Using Resin-Supported Peptide Having a Polyleucine Tether. Org. Lett 2008, 10, 2035–2037. [PubMed: 18407642]

12. (a)Jacobsen EN; Pfaltz A; Yamamoto H, Eds. Comprehensive Asymmetric Catalysis I–III Springer-Verlag: Heidelberg, 1999.(b)Ojima I, Ed. Catalytic Asymmetric Synthesis; Wiley-VCH: New York, 2000.

13. (a)For select examples, see: Knowles WS; Sabacky MJ Catalytic Asymmetric Hydrogenation Employing a Soluble, Optically Active, Rhodium Complex. Chem. Commun 1968, 1445–1446. (b)Miyashita A; Yasuda A; Takaya H; Toriumi K; Ito T; Souchi T; Noyori R Synthesis of 2,2'-Bis(diphenylphosphino)-1,1'-binaphthyl (BINAP), an Atropisomeric Chiral Bis(triaryl)phosphine, and its Use in the Rhodium(I)-Catalyzed Asymmetric Hydrogenation of α-(Acylamino)acrylic Acids. J. Am. Chem. Soc 1980, 102, 7932–7934.(c)Ikariya T; Blacker AJ Asymmetric Transfer Hydrogenation of Ketones with Bifunctional Transition Metal-Based Molecular Catalysts. Acc. Chem. Res 2007, 40, 1300–1308. [PubMed: 17960897]

14. (a)For select examples, see: Procházková E; Kolmer A; Ilgen J; Schwab M; Kaltschnee L; Fredersdorf M; Schmidts V; Wende RC; Schreiner PR; Thiele CM Uncovering Key Structural Features of an Enantioselective Peptide-Catalyzed Acylation Utilizing Advanced NMR Techniques. Angew. Chem. Int. Ed 2016, 55, 15754–15759.(b)Schnitzer T; Wennemers H Influence of the Trans/Cis Conformer Ratio on the Stereoselectivity of Peptidic Catalysts. J. Am. Chem. Soc 2017, 139, 15356–15362. [PubMed: 29043799]

15. Klausen RS; Kennedy CR; Hyde AM; Jacobsen EN Chiral Thioureas Promote Enantioselective Pictet–Spengler Cyclization by Stabilizing Every Intermediate and Transition State in the Carboxylic Acid-Catalyzed Reaction. J. Am. Chem. Soc 2017, 139, 12299–12309. [PubMed: 28787140]

16. Abascal NC; Miller SJ Solution Structures and Molecular Associations of a Peptide-Based Catalyst for the Stereoselective Baeyer–Villiger Oxidation. Org. Lett 2016, 18, 4646–4649. [PubMed: 27588823]

17. Diener ME; Metrano AJ; Kusano S; Miller SJ Enantioselective Synthesis of 3-Arylquinazolin-4(3H)-ones via Peptide-Catalyzed Atroposelective Bromination. J. Am. Chem. Soc 2015, 137, 12369–12377. [PubMed: 26343278]

18. (a)Metrano AJ; Abascal NC; Mercado BQ; Paulson EK; Miller SJ Structural studies of β-turncontaining peptide catalysts for atroposelective quinazolinone bromination. Chem. Commun 2016, 52, 4816–4819.(b)Metrano AJ; Abascal NC; Mercado BQ; Paulson EK; Hurtley AE; Miller SJ Diversity of Secondary Structure in Catalytic Peptides with β-Turn-Biased Sequences. J. Am. Chem. Soc 2017, 139, 492–516. [PubMed: 28029251]

19. (a)Tantillo DJ Faster, Catalyst! React! React! Exploiting Computational Chemistry for Catalyst Development and Design. Acc. Chem. Res 2016, 49, 1079. [PubMed: 27323885] (b)Walden DM; Ogba OM; Johnston RC; Cheong PH-Y Computational Insights into the Central Role of Nonbonding Interactions in Modern Covalent Organocatalysis. Acc. Chem. Res 2016, 49, 1279–1291. [PubMed: 27267964] (c)Wheeler SE; Seguin TJ; Guan Y; Doney AC Noncovalent Interactions in Organocatalysis and the Prospect of Computational Catalyst Design. Acc. Chem. Res 2016, 49, 1061–1069. [PubMed: 27110641] (d)Houk KN; Liu F Holy Grails for Computational Organic Chemistry and Biochemistry. Acc. Chem. Res 2017, 50, 539–543. [PubMed: 28945400]

20. Thiel W Computational Catalysis—Past, Present, and Future. Angew. Chem. Int. Ed 2014, 53, 8605–8613.

21. (a)For select computational studies of peptide-based catalysts, see: Harriman DJ; Deslongchamps G Reverse-docking as a computational tool for the study of asymmetric organocatalysis. J. Comp.-Aided Mol. Des 2004, 18, 303–308.(b)Hammar P; Córdova A; Himo F Density functional theory study of the stereoselectivity in small peptide-catalyzed intermolecular aldol reactions. Tetrahedron: Asymmetry 2008, 19, 1617–1621.(c)Osuna S; Dermenci A; Miller SJ; Houk KN The Roles of Counterion and Water in a Stereoselective Cysteine-Catalyzed Rauhut–Currier Reaction: A Challenge for Computational Chemistry. Chem.—Eur. J 2013, 19, 14245–14253. [PubMed: 24038400] (d)Liao R-Z; Santoro S; Gotsev M; Marcelli T; Himo F Origins of Stereoselectivity in Peptide-Catalyzed Kinetic Resolution of Alcohols. ACS Catal 2016, 6, 1165–1171.

22. (a)Gustafson JL; Sigman MS; Miller SJ Linear Free-Energy Relationship Analysis of a Catalytic Desymmetrization Reaction of a Diarylmethane-bis(phenol). Org. Lett 2010, 12, 2794–2797. [PubMed: 20486656] (b)Milo A; Bess EN; Sigman MS Interrogating Selectivity in Catalysis Using Molecular Vibrations. Nature, 2014, 507, 210–214. [PubMed: 24622199] (c)Sigman MS; Harper KC; Milo A The Development of Multidimensional Analysis Tools for Asymmetric Catalysis and Beyond. Acc. Chem. Res 2016, 49, 1292–1301. [PubMed: 27220055]

23. Crawford JM; Stone EA; Metrano AJ; Miller SJ; Sigman MS Parameterization and Analysis of Peptide-Based Catalysts for the Atroposelective Bromination of 3-Arylquinazolin-4(3H)-ones. J. Am. Chem. Soc 2018, 140, 868–871. [PubMed: 29300461]

24. Phillips JC; Braun R; Wang W; Gumbart J; Tajkhorshid E; Villa E; Chipot C; Skeel RD; Kalé L; Schulten K Scalable Molecular Dynamics with NAMD. J. Comput. Chem 2005, 26, 1781–1802. [PubMed: 16222654]

25. Stone JE; Phillips JC; Freddolino PL; Hardy DJ; Trabuco LG; Schulten K Accelerating Molecular Modeling Applications with Graphics Processors. J. Comput. Chem 2007, 28, 2618–2640. [PubMed: 17894371]

26. Robertson MJ; Tirado-Rives J; Jorgensen WL Improved Peptide and Protein Torsional Energetics with the OPLS-AA Force Field. J. Chem. Theory Comput 2015, 11, 3499–3509. [PubMed: 26190950]

27. Jorgensen WL; Maxwell DS; Tirado-Rives J Development and Testing of the OPLS All-Atom Force Field on Conformational Energetics and Properties of Organic Liquids. J. Am. Chem. Soc 1996, 118, 11225–11236

28. Dodda LS; Vilseck JZ; Tirado-Rives J; Jorgensen WL 1.14*CM1A-LBCC: Localized Bond-Charge Corrected CM1A Charges for Condensed-Phase Simulations. J. Phys. Chem. B 2017, 121, 3864–3870. [PubMed: 28224794]

29. Dodda LS; Cabeza de Vaca I; Tirado-Rives J; Jorgensen WL LigParGen Web Server: An Automatic OPLS-AA Parameter Generator for Organic Ligands. Nucleic Acids Res 2017, 45, W331–W330. [PubMed: 28444340]

30. Feller SE; Zhang Y; Pastor RW; Brooks BR Constant Pressure Molecular Dynamics Simulation: The Langevin Piston Method. J. Chem. Phys 1995, 103, 4613–4621.

31. Darden T; York D; Pedersen L Particle Mesh Ewald: An N·log(N) Method for Ewald Sums in Large Systems. J. Chem. Phys 1993, 98, 10089–10092.

32. Miyamoto S; Kollman PA SETTLE: An Analytical Version of the SHAKE and RATTLE Algorithm for Rigid Water Models. J. Comput. Chem 1992, 13, 952–962.

33. Trott O; Olson AJ AutoDock Vina: Improving the Speed and Accuracy of Docking with a New Scoring Function, Efficient Optimization, and Multithreading. J. Comput. Chem 2010, 31, 455–461. [PubMed: 19499576]

34. Arthur D; Vassilvitskii S K-Means++: The Advantages of Careful Seeding In Proceedings of the Eighteenth Annual ACM-SIAM Symposium on Discrete Algorithms, Society for Industrial and Applied Mathematics: New Orleans, Louisiana, 2007; pp 1027–1035.

35. Zhang T; Ramakrishnan R; Livny M BIRCH: An Efficient Data Clustering Method for Very Large Databases In Proceedings of the 1996 ACM SIGMOD International Conference on Management of Data; ACM: Montreal, Quebec, Canada, 1996; pp 103–114.

36. Pedregosa F; Varoquaux G; Gramfort A; Michel V; Thirion B; Grisel O; Blondel M; Prettenhofer P; Weiss R; Dubourg V; Vanderplas J; Passos A; Cournapeau D; Brucher M; Perrot M; Duchesnay E Scikit-Learn: Machine Learning in Python. J. Mach. Learn. Res 2011, 12, 2825–2830.

37. MacQueen J MacQueen J Some Methods for Classification and Analysis of Multivariate Observations. Proc. Fifth Berkeley Symp. on Math. Statist. and Prob 1967, 1, 281–297.

38. Steiner T The Hydrogen Bond in the Solid State. Angew. Chem. Int. Ed 2002, 41, 48–76.

39. (a)For example, see: Denmark SE; Burk MT Lewis Base Catalysis of Bromo- and Iodolactonization, and Cycloetherification. Proc. Natl. Acad. Sci. U.S.A 2010, 107, 20655–20660. For a comprehensive overview of Lewis base catalysis, see: [PubMed: 20705900] (b)Denmark SE; Beutner GL Lewis Base Catalysis in Organic Synthesis. Angew. Chem. Int. Ed 2008, 47, 1560–1638.

40. (a)Barriers were computed at the M06-2X/6-311++G(2d,3p)//B3LYP/6-31+G(d,p) level of theory using *Gaussian 09* Gaussian 09, Revision C.01, Frisch MJ; Trucks GW; Schlegel HB; Scuseria GE; Robb MA; Cheeseman JR; Scalmani G; Barone V; Mennucci B; Petersson GA; Nakatsuji H; Caricato M; Li X; Hratchian HP; Izmaylov AF; Bloino J; Zheng G; Sonnenberg JL; Hada M; Ehara M; Toyota K; Fukuda R; Hasegawa J; Ishida M; Nakajima T; Honda Y; Kitao O; Nakai H; Vreven T; Montgomery JA, Jr; Peralta JE; Ogliaro F; Bearpark M; Heyd JJ; Brothers E; Kudin KN; Staroverov VN; Kobayashi R; Normand J; Raghavachari K; Rendell A; Burant JC; Iyengar SS; Tomasi J; Cossi M; Rega N; Millam JM; Klene M; Knox JE; Cross JB; Bakken V; Adamo C; Jaramillo J; Gomperts R; Stratmann RE; Yazyev O; Austin AJ; Cammi R; Pomelli C; Ochterski JW; Martin RL; Morokuma K; Zakrzewski VG; Voth GA; Salvador P; Dannenberg JJ; Dapprich S; Daniels AD; Farkas Ö; Foresman JB; Ortiz JV; Cioslowski J; Fox DJ Gaussian, Inc, Wallingford CT, 2009.(b)Zhao Y; Truhlar DG The M06 Suite of Density Functionals for Main Group Thermochemistry, Thermochemical Kinetics, Noncovalent Interactions, Excited States, and Transition Elements: Two New Functionals and Systematic Testing of Four M06-Class Functionals and 12 Other Functionals. Theor. Chem. Acc 2008, 120, 215–241.

41. Peter C; Daura X; van Gunsteren WF Calculation of NMR-Relaxation Parameters for Flexible Molecules from Molecular Dynamics Simulations. J. Biomol. NMR 2001, 20, 297–310. [PubMed: 11563554]

42. Feenstra KA; Peter C; Scheek RM; van Gunsteren WF; Mark AE Comparison of Methods for Calculating NMR Cross-Relaxation Rates (NOESY and ROESY Intensities) in Small Peptides. J. Biomol. NMR 2002, 23, 181–194. [PubMed: 12238590]

43. Chalmers G; Glushka JN; Foley BL; Woods RJ; Prestegard JH Direct NOE Simulation from Long MD Trajectories. J. Magn. Reson 2016, 265, 1–9. [PubMed: 26826977]
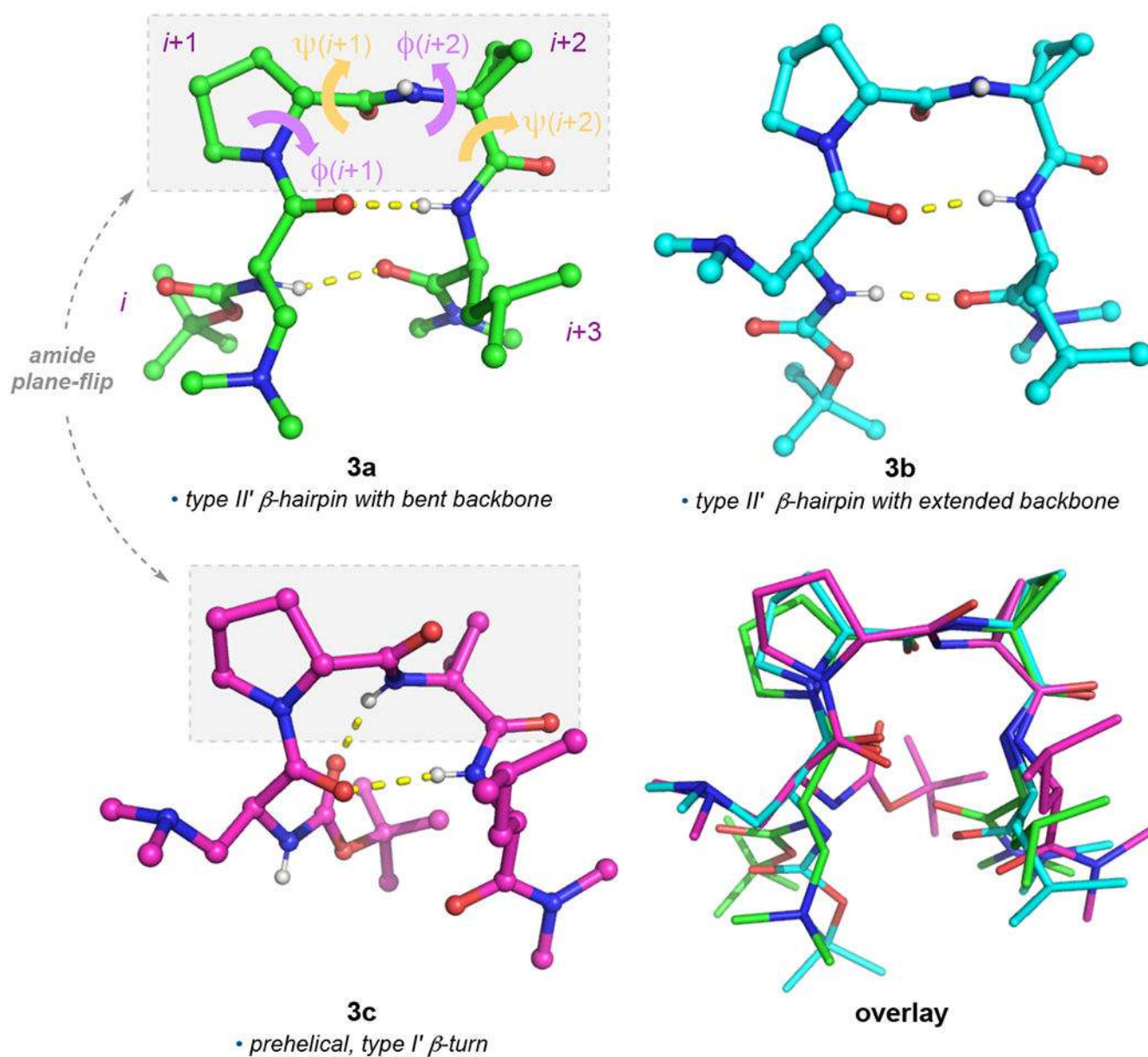
Figure 1.
Three distinct conformers of peptide **3** observed in crystal structures. Based on the ϕ and ψ dihedrals of the loop region residues and the internal H-bonding network, conformers **3a** and **3b** are classified as type II′ β-hairpins. Conformer **3c** classifies as a type I′ β-turn that is pre-helical in geometry.
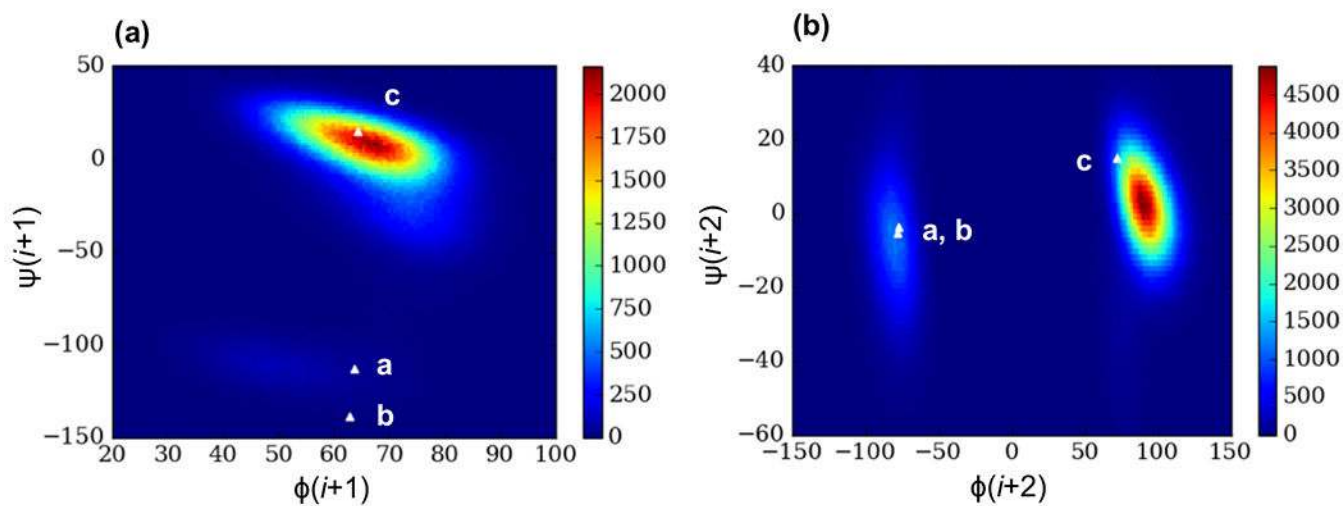
Figure 2.
Joint distribution plots of backbone dihedral angles ϕ and ψ in the (a) i+1 and (b) i+2 residues of peptide **3** from MD simulations in benzene. The crystallographic values are marked by triangles.
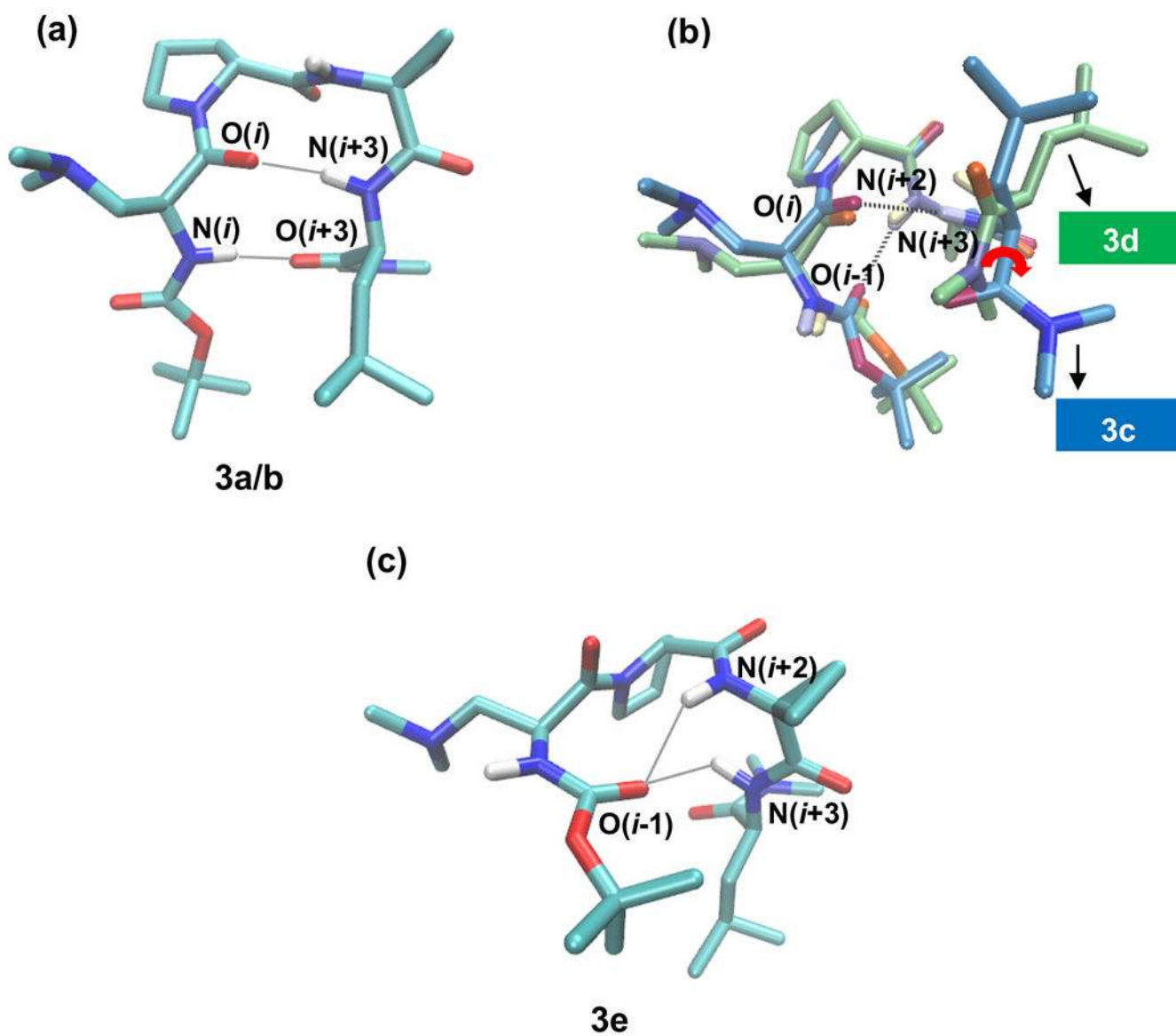
Figure 3.
Representative structures of the confonners identified from the cluster analysis: (a)
Conformer **3a/b**, (b) overlay of confonners **3c** (blue) and **3d** (green), and (c) confonner **3e**.
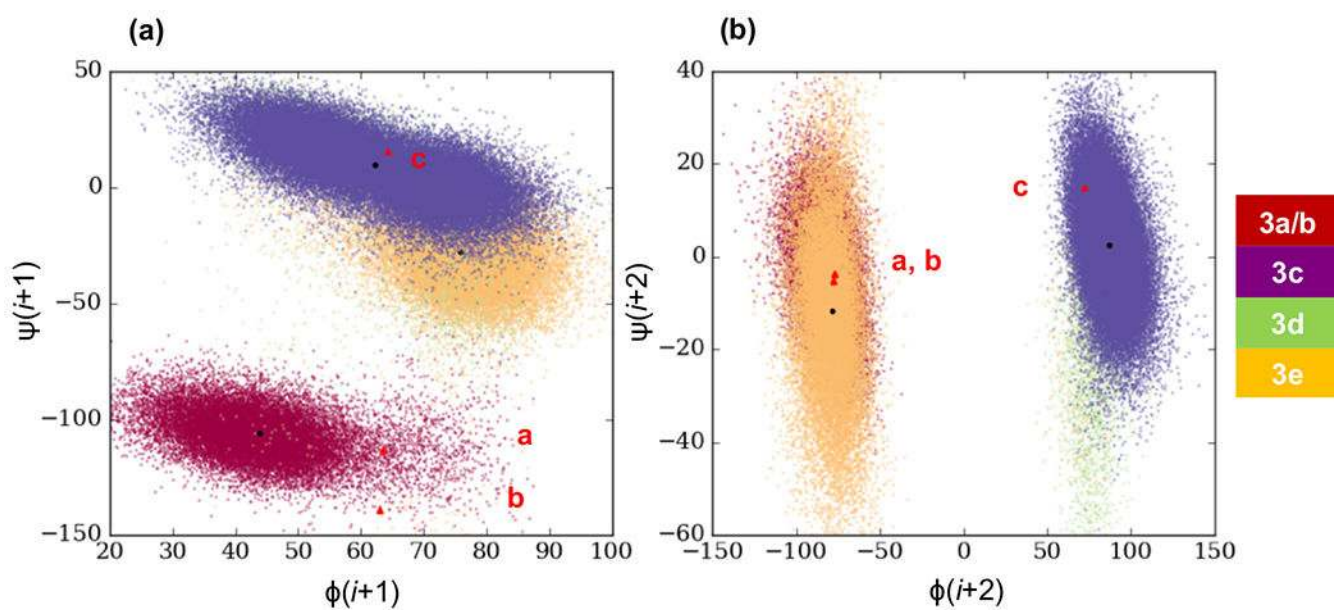
Figure 4.
Scatter plots of backbone dihedral angles ϕ and ψ in the (a) *i*+1 and (b) *i*+2 residues of peptide **3** from MD simulations in benzene (colored according to cluster). The crystallographic values and centroids of clusters are denoted by red triangles and black dots, respectively.
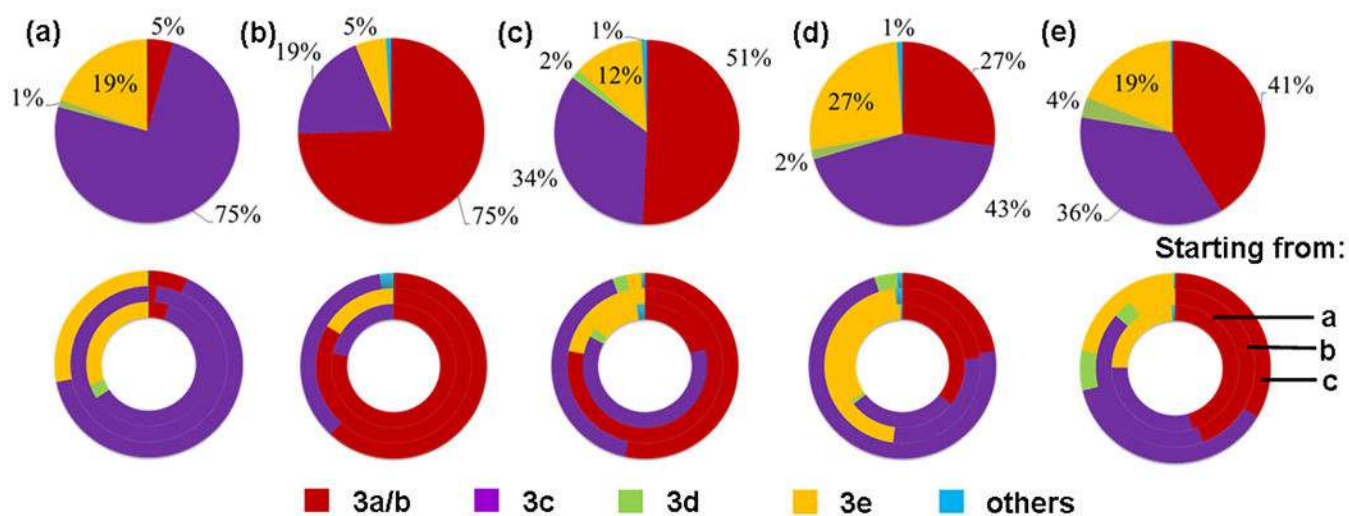
Figure 5.
Conformational composition from cluster analysis. (a) Peptide **3** alone in benzene. (b) Peptide **3** in the presence of substrate (a*S*)-**1a**. (c) Peptide **3** in the presence of substrate (a*S*)-**1b**. (d) Peptide **3** in the presence of substrate (a*R*)-**1a**. (e) Peptide **3** in the presence of substrate (a*R*)-**1b**.
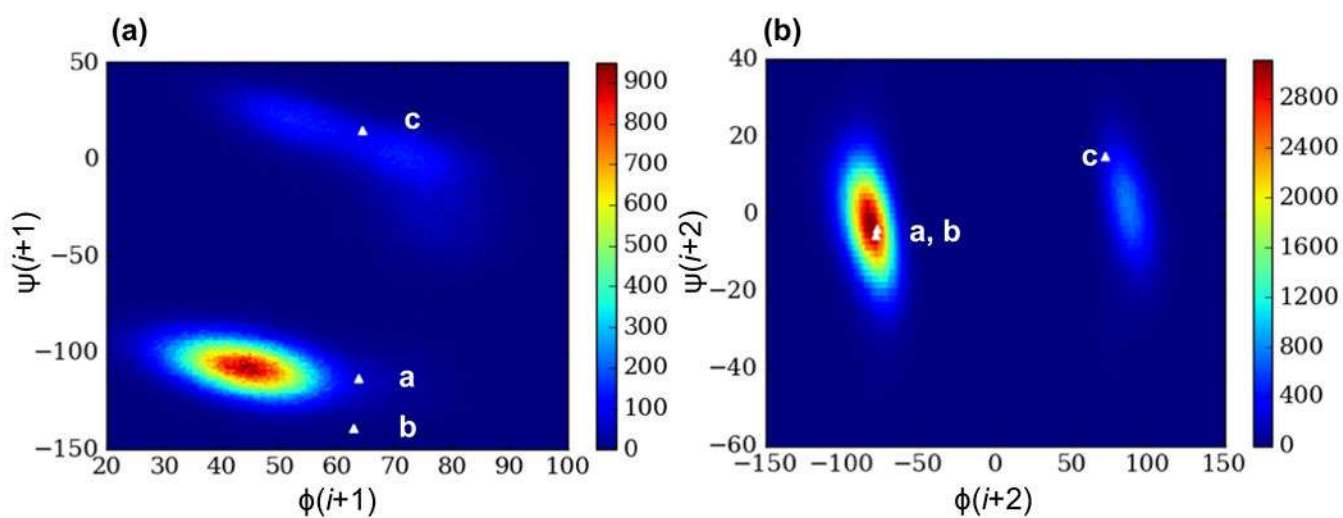
Figure 6.
Joint distribution plots of backbone dihedral angles ϕ and ψ in the (a) *i*+1 and (b) *i*+2 residues of peptide **3** in the presence of substrate (a*S*)-**1a** from MD simulations in benzene. The crystallographic values are marked by triangles.
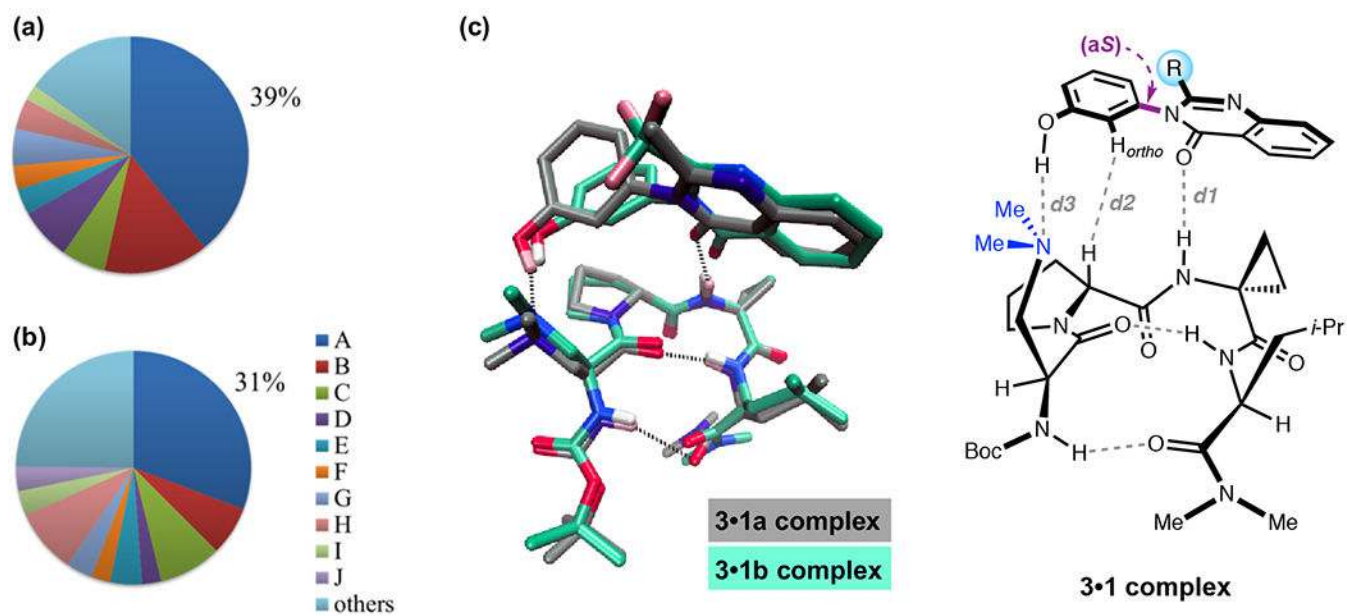
Figure 7.
Composition of binding poses in the cluster analysis of (a) **3+1a** complex and (b) **3+1b** complex. (c) Overlay of binding pose A in the **3+1a** (grey) and **3+1b** (cyan) complexes.
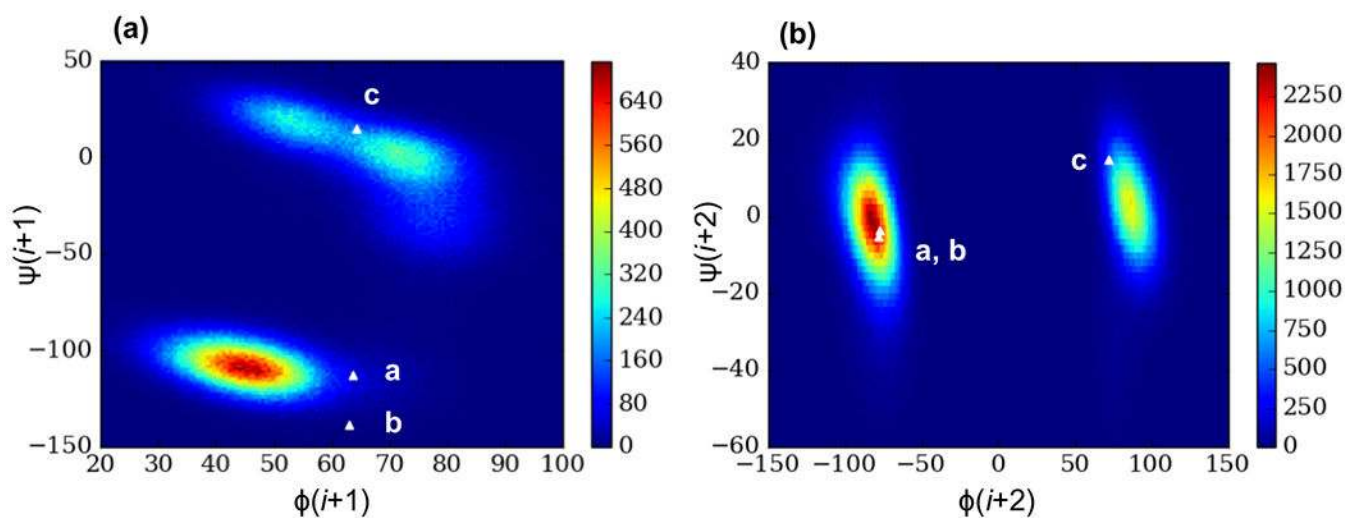
Figure 8.
Joint distribution plots of backbone dihedral angles ϕ and ψ in the (a) i+1 and (b) i+2 residues of peptide **3+1b** from MD simulations in benzene. The crystallographic values are marked by triangles.
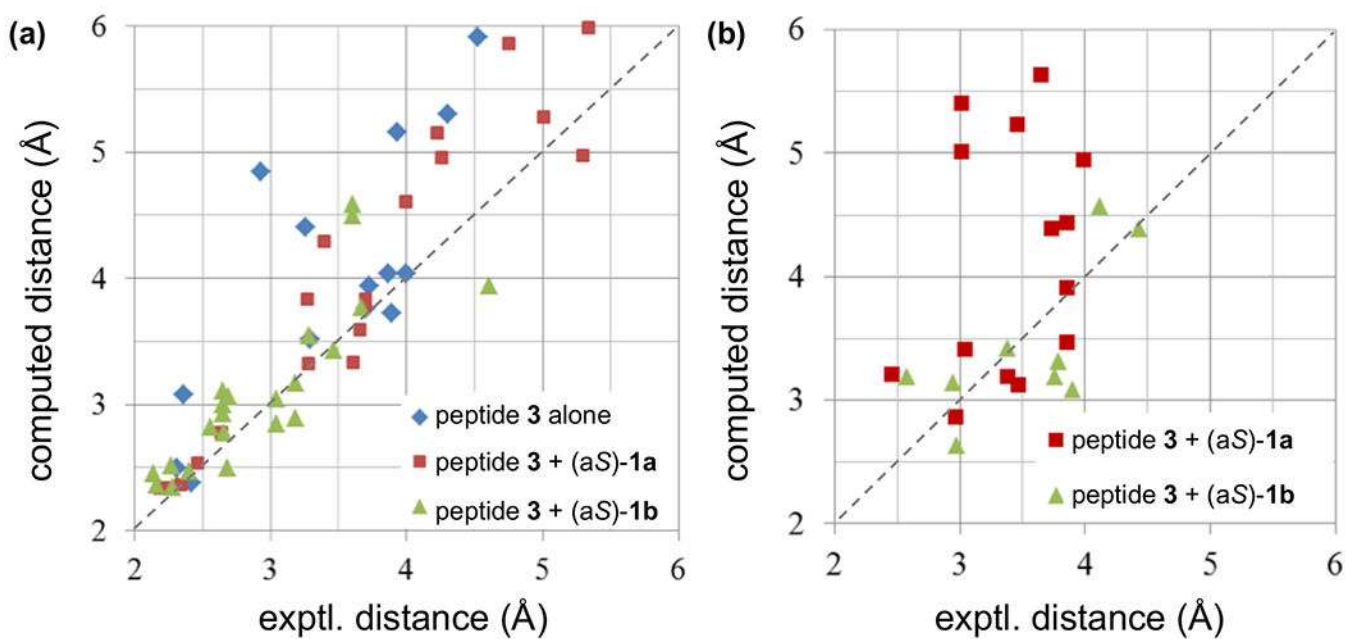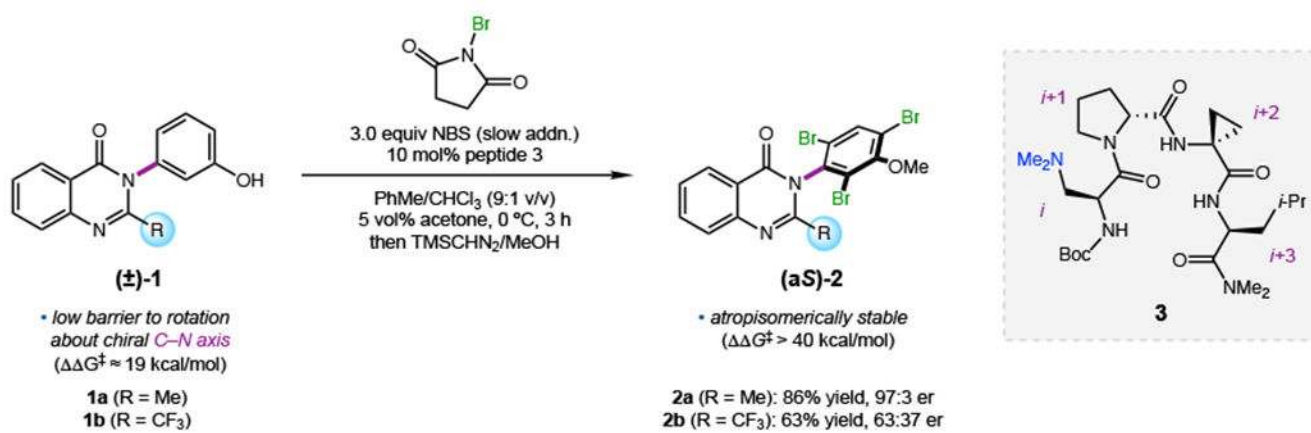
Figure 9.
Plot of through-space distances from NOESY measurements versus simulations, (a)
Intramolecular interactions in peptide **3**. (b) Internnolecular interactions between peptide **3**
and substrates in binding pose A.

Scheme 1.
Peptide-catalyzed, atroposelective bromination of 3-arylquinazolin-4(3*H*)-ones **1**.

Table 1.

Key Intermolecular Distances (in Å) in Different Binding Poses of the **3+1a** Complex

binding pose	*d1:* N(Acpc)⋯O=C(1a)	*d2:* α(Pro)⋯H*ortho*(1a)	*d3:* N$_\gamma$(Dmaa)⋯HO(1a)
A	3.18±1.18	3.73±1.05	3.26±1.58
B	8.94±2.36	6.23±2.58	6.51±2.38
C	12.36±4.44	10.09±4.63	7.54±5.05
D	11.77±3.78	10.04±4.09	6.89±4.25
E	9.55±2.72	8.25±3.10	8.72±3.93
F	6.55±3.48	6.16±3.58	7.54±3.90
G	10.39±4.58	10.76±5.08	13.33±5.36
H	8.92±3.80	8.06±4.24	11.46±4.88
I	11.12±4.07	12.12±4.89	13.51±5.43